Understanding the High Performance of over 15% Efficiency in Single-Junction Bulk Heterojunction Organic Solar Cells

Akchheta Karki, Joachim Vollbrecht, Alana L Dixon, Nora Schopp, Max Schrock, G N Manjunatha Reddy, Thuc-quyen Nguyen

Article type: Communication

Understanding the High Performance of over 15% Efficiency in Single-Junction Bulk Heterojunction Organic Solar Cells

Akchheta Karki, Joachim Vollbrecht, Alana L. Dixon, Nora Schopp, Max Schrock, G. N. Manjunatha Reddy, Thuc-Quyen Nguyen**

((Optional Dedication))

Prof. T.-Q. N, A. K., Dr. J. V. A. L. D., N. S., M. S.

Center for Polymers and Organic Solids, University of California Santa Barbara (UCSB), Santa Barbara, CA 93106, USA
E-mail: quyen@chem.ucsb.edu

Dr. G. N. M. R.

University of Lille, CNRS, Centrale Lille, ENSCL, Univ. Artois, UMR 8181, Unité de Catalyse et Chimie du Solide, F-59000, France

E-mail: gnm.reddy@univ-lille.fr

Keywords: organic photovoltaics, recombination, charge extraction, low voltage losses, solid-state NMR

Abstract

The highly efficient single-junction bulk-heterojunction (BHJ) PM6:Y6 system can achieve high open circuit voltages (V_{OC}) while maintaining exceptional fill-factor (*FF*) and short-circuit current (J_{SC}) values. With a low energetic offset, the blend system was found to exhibit radiative and non-radiative recombination losses that are among the lower reported values in the literature. Recombination and extraction dynamic studies revealed that the device shows moderate non-geminate recombination coupled with exceptional extraction throughout the relevant operating conditions. Several surface and bulk characterization techniques were employed to understand the phase separation, long-range ordering, as well as donor:acceptor (D:A) inter- and intramolecular interactions at an atomic-level resolution. This was achieved using photo-conductive atomic force microscopy (pc-AFM), grazing incidence wide angle x-ray scattering (GIWAXS), and solid-state ^{19}F Magic-Angle Spinning (MAS) NMR spectroscopy. The synergy of multifaceted characterization and device physics was used to uncover key insights, for the first time, on the structure-property relationships of this high performing BHJ blend. Detailed information about atomically resolved D:A interactions and packing revealed that the high performance of over 15% efficiency in this blend can be correlated to a beneficial morphology that allows high J_{SC} and *FF* to be retained despite the low energetic offset.

Introduction

Polymer:non-fullerene acceptor (NFA) based single-junction organic solar cells (OSCs) have recently attained record-breaking power conversion efficiencies (*PCE*s) of over 16%.[1] Numerous

recently reported studies attribute the high performance of polymer:NFA-based OSCs to an improvement in the open-circuit voltage (V_{OC}) without significantly impeding the charge generation efficiency.[2–4] Such improvements in the V_{OC} can be credited to a rise in the number of systems with relatively low energetic offsets ($\Delta G_{S1\text{-}CT}$), which is defined as the energy difference between the charge transfer (CT) state and the singlet exciton state (S_1) of the lower bandgap component in the blend.[2,5,6] While blend systems with low energetic offsets are sought for achieving high open-circuit-voltages, such blends commonly suffer from modest short-circuit current (J_{SC}) and fill-factor (*FF*) values, which can limit the *PCE*.[5–10]

In this study, the recently reported high performing blend system PM6:Y6, was examined to obtain an in-depth understanding of the voltage losses, as well as the charge recombination and extraction dynamics. Remarkably, the PM6:Y6 blend is simultaneously able to achieve high V_{OC} (0.825V) with exceptional *FF* (74%) and J_{SC} (25.2 mA/cm^2) values, which is likely linked to a favorable morphology. Therefore, to gain detailed insights into the morphology of the blend, three different morphology characterization techniques were used in combination to visualize the photoconductive donor and acceptor phase-separated regions on the surface of the blend film, characterize the ordering in the bulk of the blend film, and probe the D:A inter- and intramolecular interactions. This work provides key insights on the device physics and detailed morphology of the highly efficient single-junction OSC blend, while unravelling the underlying mechanisms for achieving *PCEs* of over 15 %.

The chemical structures of the donor and acceptor materials, along with the energy levels and device structure of the PM6:Y6 blend system are shown in **Figure 1**. Devices with PEDOT:PSS as the bottom electrode and solution processed PDINO layer capped with evaporated Aluminum electrodes

were optimized as reported in the previous study.[11] The *J-V* characteristics of a device at 1 sun illumination (100 mW cm^{-2} AM 1.5) is shown in **Figure S1a**. The average *PCE* in **Table S1** was obtained from testing 20 devices, and the best performing device exhibited a *PCE* of up to 15.35%. An integrated J_{SC} from the external quantum efficiency (EQE) spectra of 24.9 mA/cm^2 was obtained which is within 5 % of the average J_{SC} measured via the *J-V* characteristics of the devices at 1 sun illumination (**Figure S1b**). A combined simulation and experimental approach[12] was used to obtain an exceptional internal quantum efficiency (IQE) of over 95% over the relevant wavelength regime (500-800 nm) in this blend, suggesting highly efficient charge generation and extraction (**Figure S1b**). Furthermore, the preliminary results by Neher et. al.[13] obtained via a combination of internal generation efficiency (IGE) using time-delayed collection field (TDCF) and IQE measurements suggest that losses due to exciton harvesting and geminate recombination are minimal in this blend system. To understand what makes this blend system achieve over 15% *PCE*, we examine the individual components that make up the *PCE* (V_{OC}, *FF,* and J_{SC}) in detail.

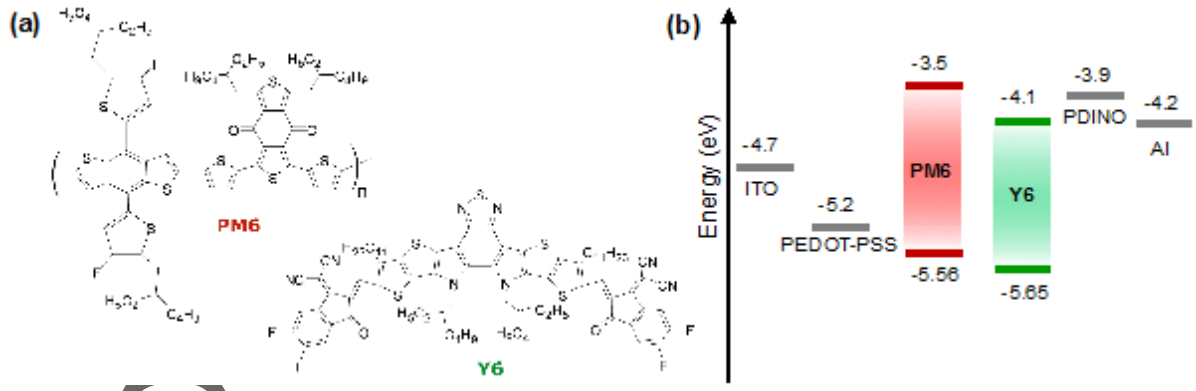

Figure 1. (a) Chemical structures of PM6 and Y6, and (b) energy levels of the different layers used in the studied devices (PM6 and Y6 based on CV measurements).

To understand the high V_{OC}, we begin by delving deeper into understanding the voltage losses in this blend. For evaluating the losses limiting the V_{OC} in this blend, we evaluate the energy loss, E_{loss} as:

$$E_{loss} = S_1 - qV_{OC}, \quad (1)$$

where, S_1 is the singlet exciton energy of the lower bandgap component in the blend and q is the elementary charge. A recently published paper by Vandewal el. al.[14] dissuades the use of ill-defined absorption onsets or HOMO and LUMO energies as reference points for evaluating voltage losses. Therefore, we adopt the optical method described in the paper[14] for a precise measurement of the singlet exciton energy. To obtain the S_1, the intersection point of the emission spectra (from electroluminescence measurements, EL) and absorption spectra (from photovoltaic external quantum efficiency measurements, EQE_{PV}) of the lower band-gap component in the blend (acceptor,

Y6) is determined (**Figure S2)**. The S_1 obtained from this method was 1.36 eV.

Losses limiting the V_{OC} can be further divided into two parts: losses due to charge transfer as defined by the difference between the S_1 and the energy of the CT state (E_{CT}), and losses due to recombination defined by the difference in E_{CT} and V_{OC}. Commonly, to identify the CT state in a blend, the EQE_{PV} is measured, and the CT state is identified as the absorption feature visible at energies lower than the bandgap of either the donor or acceptor. The E_{CT} is then determined by fitting an expression derived from Marcus theory (**Equation S1**) to the tail of the blend EQE_{PV} spectrum.[7,15] However, the CT state is not always pronounced in the low-energy tail of the EQE_{PV} spectra, especially in blends where the energetic offsets between the donor and acceptor are low (i.e., low HOMO-HOMO or LUMO-LUMO offsets)[2,5,8,16], and it can therefore be difficult to distinguish the energy of the CT state from the donor or acceptor singlet state. It is possible, however, to significantly reduce the degrees of freedom in the fitting by 1) performing a simultaneous fit to both the EQE_{PV} (**Equation S1**) and the EL (**Equation S2**) spectra[3,9,17–19] using equations derived from Marcus theory, as was first demonstrated by Vandewal *et. al.*[15] and 2) calculating the EQE_{PV} down to 10^{-7} using sensitively measured EL data and the relationship shown in **Equation S3**.[20] The added sensitivity of four orders of magnitude in the measurements allows for the deconvolution of the Gaussian-shaped CT absorption which was previously absent from the sharp absorption tail of the measured EQE data. In fact, a recently published paper[19] has shown that this method significantly lowers errors in the fitting parameters (E_{CT}, λ, f) in low energetic offset systems. Using this analysis, the E_{CT} in the PM6:Y6 blend was determined to be 1.31±0.003 eV (**Figure 2**), further confirming the low offset in this system with a difference between S_1 and E_{CT} of only ~ 0.05 eV. It is worth noting, however, that despite the reduction in degrees of freedom in the Marcus fitting, the E_{CT} value

obtained here serves only as an estimate due to the significant uncertainty that arises in separating the CT state emission and the singlet exciton emission in low energetic offset systems. Therefore, we report the CT energy in this blend – as has been done in some recently reported papers[9,19]– with a caveat that the obtained E_{CT} value is an estimate only.

Next, losses due to recombination (E_{CT} to V_{OC}), which can be divided into radiative (ΔV_{rad}) and non-radiative losses ($\Delta V_{non\text{-}rad}$), are quantified (**Equation S4**). As derived from a detailed balance analysis, about 200-250 meV of radiative recombination is needed to establish thermodynamic equilibrium.[17] In recent years, an increasing number of non-radiative recombination loss-related studies have led us to understand the nature and origin of this recombination in more detail, with studies showing that this recombination can be attributed to carbon-carbon bond vibrations[23], molecular orientation at the donor-acceptor interface[18,24], energetic driving force[3,5,9], and E_{CT} values[23]. The breakdown of the losses from S_1 to V_{OC} for this system is shown schematically in an energy loss diagram in **Figure 2** (details are described in the SI). Most notably, the total voltage loss due to recombination ($E_{CT} - V_{OC}$) is ~ 0.485 eV and is among one of the lower recombination-related loss values reported in the literature.[5,6,19,25] In addition to the radiative and non-radiative recombination contributions to the voltage losses, the contributions to the voltage losses from energetic disorder was also quantified. From an analysis of the Urbach energy (E_U) from the tail states of the EQE spectra of the blend, the PM6:Y6 system was found to have a markedly low energetic disorder, with an E_U = 26.7 meV (details in the SI, **Figure S1d**). An E_U approaching a thermal energy (~ kT) indicates that the contribution to the voltage losses in the system from energetic disorder is minimal.[7,26–29]

Similar to this blend, the suppression of non-radiative recombination losses with a decreased energetic offset has been described in several recently reported studies.[3,5,9,23] This observation has

been explained by the idea that a decreased overlap of the vibrational wave function of the CT and ground state leads to the suppression of the non-radiative recombination pathway.[23] In addition, the recent paper by Qian et. al.[5] suggests that in low energetic offset systems, hybridization of the CT state with the highly emissive S_1 state will increase the radiative ability of the CT state through the intense borrowing mechanism.[30,31] In such a case, an efficient transition from the CT state back to the S_1 state can be possible, which opens up an additional radiative relaxation pathway through the highly emissive S_1 state. From the modeling of excitonic and CT states, it was found that if the radiative relaxation channel from the highly emissive S_1 state can be made efficient in this way, the non-radiative voltage losses via the CT state should synchronously decrease.[5] To further confirm that the S_1 state (Y6) is in fact highly emissive, we measured the EQE_{EL} of the Y6 only devices (**Figure S2**f), confirming the lower non-radiative recombination ($\Delta V_{non\text{-}rad}$ = 0.242 ± 5 eV) in the acceptor-only device compared to that of the blend ($\Delta V_{non\text{-}rad}$ = 0.286 ± 3 eV eV).

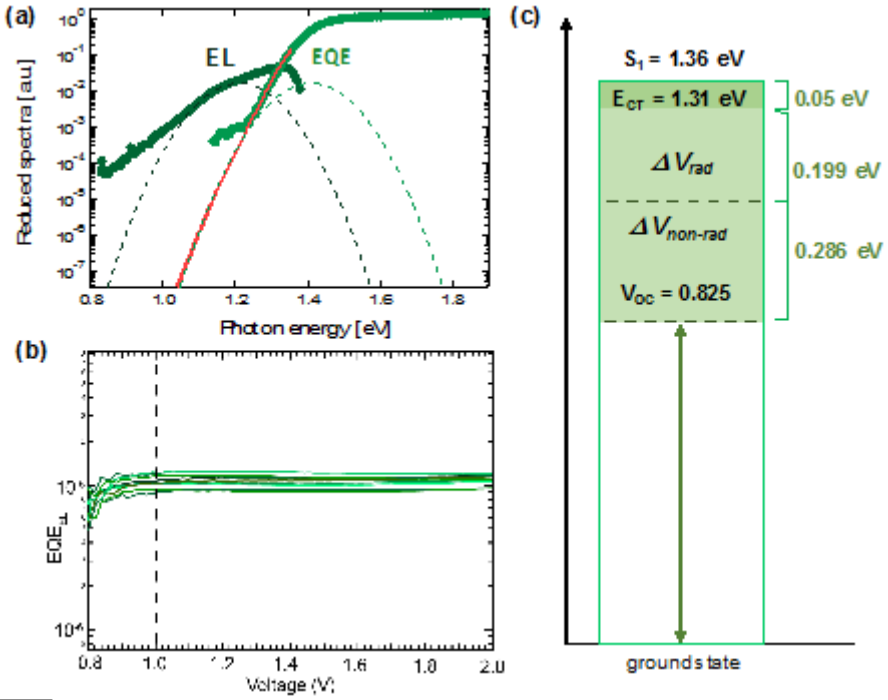

Figure 2. (a) Simultaneous fitting of the reduced EQE_{PV} and EL spectra; reciprocity relationship between EQE_{PV} and EL from **Equation S3** was used to calculate the EQE_{PV} down to 10^{-7} shown by the red solid line, the fitting parameters used were: λ = 0.10 eV, E_{CT} = 1.31 eV, $f = 3.0 \times 10^{-3}$ eV^2. (b) Measured EQE_{EL} vs. applied bias for 12 devices, where the EQE_{EL} values were extracted from the voltage at which the injected current is equal to the J_{SC} of the devices under 1 sun illumination (shown approximately by the black dotted line) and $\Delta V_{non\text{-}rad}$ was calculated from **Equation S6** after obtaining the measured EQE_{EL}. (c) Schematic representation of the breakdown of voltage losses from S_1 to V_{OC}.

In addition to the low voltage losses that help to maximize the V_{OC}, the blend system also exhibits high J_{SC} and *FF* values, which are crucial for the remarkable *PCE* of 15.35% in the best

performing device – such a combination of low voltage losses with high J_{SC} and *FF* is uncommon in the literature. To gain further insight into this, the recombination and extraction dynamics in the blend were measured and analyzed. It has been shown that if the charge extraction time is faster than or compatible to the recombination time, charge recombination can be reduced.[6,32,33] As a first step, the photocurrent density (J_{ph}) of the device is calculated using the following equation:

$$J_{ph} = J_{light} - J_{dark}, \quad (2)$$

where J_{light} is the current density measured under illumination and J_{dark} is the current density measured in the dark. The photocurrent density is plotted against the effective voltage $V_{eff} = V_0 - V_{cor}$ (**Figure S4 a,b**), where V_0 is the voltage at which $J_{ph} = 0$ ($V_0 = 0.842$ V). The corrected voltage V_{cor} can be obtained by taking into account the voltage losses over the series resistance:

$$V_{cor} = V_{app} - J \cdot R_{series}, \quad (3)$$

where V_{cor} is the corrected voltage, J is the current density, and R_{series} is the series resistance which is equal to the saturated differential resistance at forward bias (i. e. $\partial V_{app}/\partial J = \text{const.}$).[34,35] Relatively high photocurrents were achieved for the PM6:Y6 solar cells and the value of J_{ph} remains high even at comparatively low effective voltages ($V_{eff} = 0.1$ V). Subsequently, the probability of charge collection (P_C) can be estimated by analyzing the ratio between the saturated photocurrent density $J_{ph,sat}$ and the values for J_{ph} at different biases[36]:

$$P_C = \frac{J_{ph}}{J_{ph,sat}}. \quad (4)$$

Figure 3a shows that the P_C retains very high values under short-circuit ($P_{C,SC} = 97.7$ %, blue circle), and maximum power conditions ($P_{C,MP} = 91.8$ %, red cross), followed by a considerable drop

once the voltage approaches open-circuit conditions ($P_{C,OC}$ = 7.03 %), which is indicative of an exceptional charge extraction and at the same time, moderate charge carrier recombination losses. It can be deduced that geminate recombination has a negligible influence on the device performance as evidenced by the significant collection probability even at comparatively low voltages. In the next step, the PM6:Y6 solar cells were tested under varying light intensities *I* by measuring light intensity dependent short-circuit current density and open-circuit voltage in order to qualitatively determine the dominant type of non-geminate recombination (**Figure S5**). The light intensities were decreased by neutral density filters. The relationship between the J_{SC} and *I* ($J_{SC} \propto I^{\alpha}$) has been used to calculate the exponent of α = 0.92 ± 0.02. Since the devices show exceptional charge extraction under short-circuit conditions ($P_{C,SC}$ = 97.7 %), it can be hypothesized that the influence of bimolecular recombination on the J_{SC} is limited. Furthermore, it should be noted that deviations in the exponent (α < 1) can also be caused by space charge effects.[37,38] Overall, these considerations constrain the predictive abilities of this type of measurement on the recombination dynamics. To better understand the recombination processes, the relationship between the V_{OC} and the light intensity *I* was also determined.[39] The V_{OC}-ln(*I*)-plot exhibits a slope of *s* = 1.02 ± 0.03 *kT*/*q*, where *k* is the Boltzmann constant, *T* is the absolute temperature (*T* = 300 K), and *q* is the elementary charge. In order to rule out the effect of leakage on the slope of the V_{OC}-ln(*I*)-plot, the *J*-*V* curves at different light intensities were plotted and analyzed (**Figure S5c,d)**. These results indicate that bimolecular recombination is the dominant recombination mechanism. However, other types of recombination such as bulk (*s* > 1 *kT*/*q*) and surface trap-assisted (*s* < 1 *kT*/*q*) recombination should also be taken into account as loss mechanisms, most notably because the opposite influence of surface and bulk trap-assisted recombination on the slope *s* could cause slopes of *s* ≈ 1 *kT*/*q*, which

could be falsely attributed to pure bimolecular recombination.[40] Therefore, a more in-depth analysis based on capacitance spectroscopy was carried out to obtain quantitative results.[35,41,42]

The capacitance of the PM6:Y6 BHJ, C_b, was used to determine the charge carrier density n and the effective mobility μ_{eff} of the studied solar cell under any operating conditions (**Figures S6 and S8;** a detailed description of obtaining the effective mobility is provided in the SI).[33,43] Under forward bias conditions, a carrier density of $n > 10^{17}$ cm^{-3} was observed, placing the carrier density in this system at the upper end of high performing NFA blends.[44] Additionally, the effective mobility ($\mu_{eff} \approx 1 \times 10^{-4}$ cm^{2}V^{-1}s^{-1}) determined using the procedure described in the SI is comparable to other high performing NFA as well as fullerene blend systems.[33] As a starting point in the quantitative analysis of the non-geminate recombination dynamics, it is assumed that the recombination current density ($J_{rec} = J_{ph,sat} - J_{ph}$) is a superposition of the three aforementioned recombination mechanisms:

$$J_{rec} = J_{bm} + J_{t,b} + J_{t,s} = qL\left(\frac{n}{\tau_{bm}} + \frac{n}{\tau_{t,b}} + \frac{n}{\tau_{t,s}}\right) = qL\left(k_{bm}n^2 + k_{t,b}n + k_{t,s}(V_{OC})\right). \quad (5)$$

Here L is the active layer thickness, τ is the charge carrier lifetime, and k is the recombination coefficient of the three different recombination mechanisms (bm: bimolecular; t,b: bulk trap-assisted; t,s: surface trap-assisted). It was possible to obtain the recombination coefficients by reconstructing the recombination current density obtained using the *J-V* characteristics from the charge carrier density (n) and the effective mobility (μ_{eff}) (**Figure S8**). The carrier density, effective mobility, voltage, and dielectric constants were used as input parameters, while the reduction factor (ξ), bulk-trap density ($N_{t,b}$), and surface-trap density ($N_{t,s}$) were the fitting parameters. Based on these results, it can be confirmed that bimolecular recombination is the dominant non-geminate recombination mechanism, while bulk trap-assisted recombination is negligible, and surface trap-

assisted recombination has only a very limited contribution at high forward biases.[45] Overall, the dependence of bimolecular recombination on the applied bias and the charge carrier density is less pronounced and the values for the respective coefficients are relatively small (k_{bm} = 3.0 – 5.8 × 10^{-13} cm^3/s) in comparison to other high performing NFAs and up to one order of magnitude lower than that for high performing fullerene solar cells.[33,46] In addition, open-circuit voltage decay (OCVD) measurements (also referred to as transient photovoltage decay) were conducted as a second technique to analyze and confirm the recombination dynamics, since other approaches relying on the electron and hole mobility determined via SCLC are not viable due to the questionable electron mobility values in the blend (**Figure S9**).[47,48] This technique yields a higher value for the bimolecular recombination coefficient when compared to the results obtained from the capacitance spectroscopy analysis ($k_{bm,OCVD}$ = (4.54 ± 0.15) · 10^{-12} cm^3/s vs. $k_{bm,CS}$ = 3.0 – 5.8 · 10^{-13} cm^3/s). However, such a trend (i.e. $k_{bm,OCVD} > k_{bm,CS}$) between these two types of measurement techniques has been observed and reported in previous studies for fullerene and NFA solar cells.[33,42] Nonetheless, the extraction of charge carriers has to also be quantified to obtain a comprehensive understanding of the processes in the studied devices.

To gain quantitative insights into the charge carrier extraction dynamics, the effective extraction time, τ_{ex}, was determined under the assumption that a charge carrier needs to traverse, on average, half of the PM6:Y6 active layer thickness until it reaches one of the electrodes. Furthermore, the active layer is treated as an effective medium[32] and the following relationship was used:

$$\tau_{ex} = \frac{qLn}{J}, \quad (6)$$

where *L* is the active layer thickness, *q* is the elementary charge, *n* is the charge carrier density, and *J* is the current density obtained from the *J*-*V* curves (details are given in the SI, **Equations S22-S24**). The effective extraction time τ_{ex} can then be directly compared to the effective charge carrier lifetime τ_{rec}, which can be accessed by re-arranging **Equation 5** (**Figure 3b**).[42] Interestingly, extraction is at least two orders of magnitude faster than recombination over most of the operating conditions. Only at high forward biases, approaching V_{OC}, do the effective extraction and charge carrier lifetimes converge. This observation correlates well with the high photocurrents J_{ph} and collection probabilities P_C retained under forward bias, as displayed in **Figure 3a**. In addition, the voltage dependent competition factor θ was calculated by taking the ratio of the effective extraction and recombination times ($\theta = \tau_{ex}/\tau_{rec}$) (**Figure 3c**).[32] A smaller competition factor has been shown to correlate to higher *FF*.[32,33] In essence, the collection probability P_C and the quantitative analysis based on capacitance spectroscopy show that the PM6:Y6 BHJ device exhibits exceptional extraction coupled with moderate bimolecular recombination losses, which is the basis for the high *FF* and J_{SC} observed. While the detailed analyses of extraction and recombination processes in PM6:Y6 provide sufficient evidence on the bulk electronic characteristics, much of these favorable charge carrier properties are expected to originate from the BHJ morphology. To confirm this, we carried out detailed morphological and structural characterizations of the PM6:Y6 blend at different length scales.

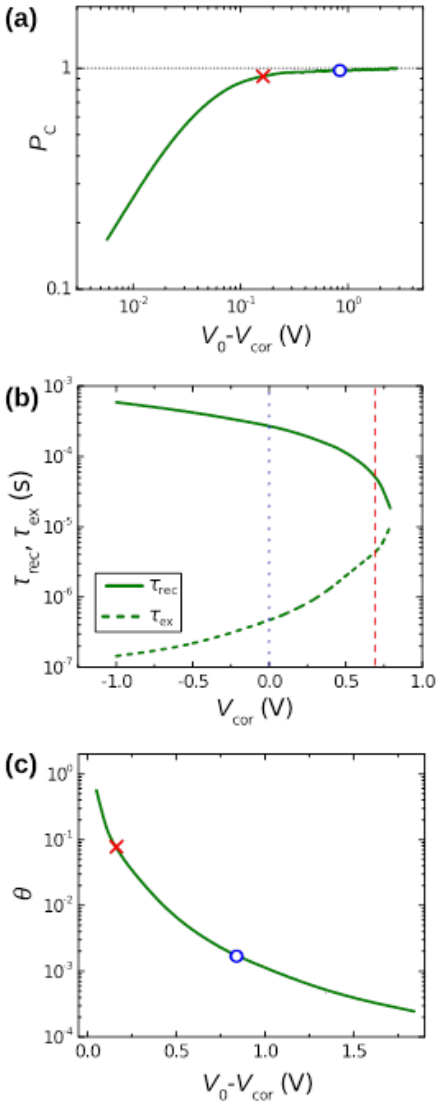

Figure 3. (a) Collection probability P_C, (b) charge carrier lifetime τ_{rec} and extraction time τ_{ex}, as well as (c) voltage dependent competition factor θ of the investigated solar cells. Short-circuit (blue circle) and maximum power (red cross) conditions are highlighted by the blue and red dotted vertical lines in (b), respectively.

The BHJ morphology has a significant influence on the device performance.[6,49–51] To gain detailed insights into the morphology of the PM6:Y6 blend at different length scales, three different techniques were used: photo-conductive atomic force microscopy (pc-AFM, sub-μm to μm) for visualizing the photoconductive hole and electron rich domains on the film surface, Grazing-Incidence Wide-Angle X-ray Scattering (GIWAXS) for probing the long-range structural order (ca. 100's nm) in the bulk of the blend film, and one and two dimensional (1D, 2D) solid-state-NMR for elucidating the D:A inter- and intramolecular interactions at sub-nm to nm distances. In a pc-AFM measurement, an electrically conductive Platinum-Chromium coated tip was used to scan the surface of photoactive layers using a white light source, which allows to map out the photo-responsive features in the PM6:Y6 blend films. The topography images (**Figure S10a,b**) show features amounting to small root-mean-square (RMS) roughness values (~ 0.8 nm) and the photocurrent image (**Figure S10c,d**) reveals small phase separated domain sizes (ranging from 20-30 nm) of hole (PM6) and electron rich (Y6) regions on the film surface in comparison to other reported blends.[6,51–54] Such a small degree of phase separation can explain the efficient charge separation and moderate recombination in the blend.[39,49,55–58] Next, in order to characterize the ordered regions in the PM6:Y6 blend film, we investigated the GIWAXS of the blend film **(**Supporting Information, **Figure S11)**. As was also previously reported for this blend[11], the GIWAXS pattern of PM6:Y6 showed that the blend displays face-on orientation which can be beneficial for charge transport in the direction normal to the substrate surface.[59,60] A detailed discussion of the GIWAXS analyses in the blend can be found in the SI.

Several theoretical and experimental studies have suggested that the nature of the D:A interactions can affect the rates of charge transfer and recombination[24,61,62], electronic coupling[18],

charge generation[18,61], and charge delocalization[63] — all of which can in turn influence the loss mechanisms in an OSC. While the correlation between the D:A interactions in a blend and bulk optoelectronic properties can be highly useful to understand the device performance, it is rarely studied for polymer:NFA-based BHJs. Here, solid-state ^{19}F MAS NMR spectroscopy has been employed to obtain atomic-level insights about the inter- and intramolecular interactions of the PM6:Y6 BHJ films. Solid-state NMR spectroscopy provides information on local structures and intermolecular interactions at sub-nm to nm distances, which could be related to both ordered and disordered regions of OPV blends. The isotropic chemical shifts and dipole-dipole couplings are sensitive to inter- and intramolecular interactions and relative orientations of donor and acceptor molecules in the BHJ morphologies. These interactions can be used, in particular, to measure internuclear distances in the absence of long-range structural order by measuring and analyzing heteronuclear dipolar couplings in heterogeneous soft matter materials.[51–53] For example, quantitative insights into the ordered and disordered regions in organic semiconductors and interfacial contacts in BHJs have been previously attained by solid-state NMR analyses in conjunction with X-ray scattering measurements and DFT calculations. [58,66–69]

The 1D and 2D ^{19}F MAS NMR spectra of PM6, Y6, and the PM6:Y6 blend were analyzed and compared in order to understand the changes in the local environments of ^{19}F sites in PM6 and Y6 upon BHJ formation. The intrinsic high sensitivity due to 100% natural abundance and large chemical shift range associated with ^{19}F MAS NMR enabled the local environments of ^{19}F sites in PM6 and Y6 to be distinguished and assigned (**Figure 4**). The ^{19}F signal at -131 ppm (**Figure 4a**) was attributed to local environments of ^{19}F sites in fluorinated thiophene groups of PM6 backbone moieties. In contrast, the ^{19}F MAS NMR spectrum of Y6 exhibited different distributions of signals that are only

partially resolved in the range between -115 ppm and -130 ppm (**Figure 4b**). These distributions of ^{19}F chemical shifts and signal intensities were attributed to the ^{19}F sites in different Y6 backbone structures, which is consistent with the presence of distinct structural orders that co-exist in the Y6 material as previously characterized by Yuan et. al. using GIWAXS measurements.[11] To confirm this analysis, 2D ^{19}F{^{19}F} spin-diffusion (SD) experiments[70] were carried out in order to identify and distinguish whether or not these ^{19}F pairs are spatially proximate to each other at sub-nm to nm distances (**Figure S12**). In a 2D ^{19}F{^{19}F} spin-diffusion experiment, the ^{19}F magnetization is allowed to exchange between different ^{19}F sites of spatially close ^{19}F nuclei for a given mixing period, which leads to self- and cross-correlation intensities. The self-correlation intensities at the diagonal of the 2D ^{19}F{^{19}F} correlation spectrum of Y6 acquired using shorter mixing period of 100 ms (**Figure S12**) indicate that this mixing time is not adequate enough for the magnetization exchange to occur between different ^{19}F sites. At a relatively longer mixing time of 1 s (**Figure S12b**), the cross-correlation intensities are observed between ^{19}F signals at -120 and -124 ppm confirming the exchange of magnetization between different ^{19}F sites in Y6 backbone moieties. These cross-correlation intensities at very long mixing times (> 500 ms) were expected to originate from weak ^{19}F-^{19}F dipole-dipole interactions. This further confirms the spectral assignments of signals at -120 and -124 ppm to ^{19}F sites in different endgroups of Y6 rather than two ^{19}F sites in *ortho* position to each other within the same endgroup. Otherwise strong cross-correlation intensities at much shorter mixing times due to efficient magnetization exchange between ^{19}F sites that are close to each other would be observed. To further corroborate this analysis, the ^{19}F chemical shifts of neat PM6 and Y6 moieties were compared with analogous chemical shifts in the PM6:Y6 blends (**Figure 4c**). Interestingly, the ^{19}F signals of Y6 at -120 ppm displaced towards a lower frequency and at -124

ppm displaced towards a slightly higher frequency that leads to a relatively narrow distribution of signal intensities centered at -123 ppm. This indicates the improved structural order of Y6 molecules accompanied by subtle differences in the local environments of ^{19}F sites in the fluorinated endgroups of Y6 moieties in the PM6:Y6 blend. By comparison, the ^{19}F chemical shift of fluorinated thiophene groups in the PM6 polymer remains at -131 ppm, which reveals the retained organization of the thiophene endgroups in the PM6 polymer upon blend formation with Y6. In addition, the 2D ^{19}F{^{19}F} correlation spectra of PM6:Y6 (**Figure S12c,d**) exhibited self-correlation intensities exclusively along the diagonal for the spectra recorded using short and long mixing times (100 ms, 1 s) confirming that there is no magnetization exchange between ^{19}F sites in PM6 and Y6. This rules out, at least in part, the likelihood of Y6 backbone moieties placed in between the π–π stacked PM6 polymer chains and confirms the lack of close contact between the acceptor moieties on the Y6 and the PM6 backbones.

From a combined investigation of the morphology using the aforementioned three different techniques, we can deduce important insights about the structural arrangement of the PM6:Y6 blend. Firstly, the phase separation of donor and acceptor regions at smaller length scales, as revealed by pc-AFM, results in moderate recombination and efficient charge separation in the blend. Secondly, GIWAXS measurements show that the blend displays good π-π stacking, which has been shown to be beneficial for charge transport.[59,60]. Although X-ray scattering and pc-AFM techniques are capable of unveiling such structural details at μm to 10-nm length scales, these methods do not have sufficient spatial resolution to identify atomic-level information. To this end, thirdly, solid-state ^{19}F MAS NMR analyses provide information about atomically resolved inter- and intramolecular D:A interactions. The main finding from ssNMR is that there is no close contact between the acceptor

moieties on the Y6 and the PM6 backbones. This was confirmed from the 2-D spin diffusion correlation studies, where there is clear evidence that the spins of the F atoms in the donor and acceptor do not interact with each other within a 1 nm distance. This alludes to a well-defined D:A interface. Several previously reported studies have shown that an enhanced intermixing of the donor and acceptor in a blend can be detrimental to the device performance by increasing charge recombination.[6,41,55] Therefore, the moderate recombination rates in this blend can be explained by the beneficial phase separation between the polymer and NFA, as visualized on a micron-scale by pc-AFM, and confirmed on a sub-nm to nm scale by ssNMR. The exceptional extraction observed in the devices can be attributed to two things. First, in the neat Y6, two different packing motifs were resolved with the 1D ^{19}F ssNMR. In the blend, only the signal from one of these two motifs dominates, which indicates a more uniform and structured packing of the Y6 molecules in the blend. Second, the 1D ^{19}F ssNMR results indicate that the PM6 packing remains unaffected with the addition of Y6 confirming that the order of the PM6 observed in the neat film is also retained in the blend. It is worth noting that the π-π stacking peaks of PM6 and Y6 obtained from GIWAXS, as reported in the previous literature,[11] are broad and quite close to each other to definitively distinguish if the π-π stacking peak observed in the blend is coming from PM6 or Y6. In this regard, ssNMR analyses which are sensitive to short range structures and interactions, are more informative about the details of the blend morphology. Ultimately, the exceptional extraction in the devices is due to the unencumbered pathways for sweeping out charge carriers via the retention of multiple unhindered and organized PM6 and Y6 domains.

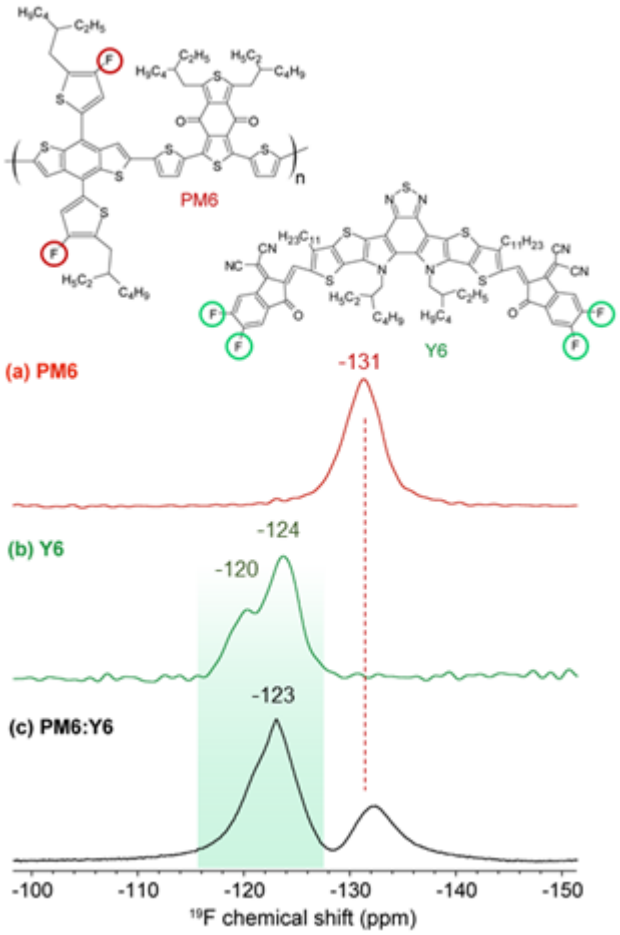

Figure 4. Solid-state ^{19}F MAS NMR spectra of (a) PM6, (b) Y6 and (c) PM6:Y6 blend acquired at 60 kHz and at room temperature. The distributions of ^{19}F chemical shifts in Y6 centered at -120 and -124 ppm were attributed to the distribution of different ^{19}F sites in different Y6 backbone structures. A narrow distribution of chemical shifts centered at -123 ppm in the PM6:Y6 blend indicates the changes in the Y6 backbone structures upon mixing with the PM6 polymer.

To summarize, the low energetic offset PM6:Y6 blend system was found to exhibit radiative and non-radiative recombination losses that are among the lower reported values in the literature

(~0.485 eV). The blend also exhibits a low energetic disorder, which further aids in reducing the voltage losses. This work shows that *PCE*s of over 15% require low voltage losses, coupled with moderate non-geminate recombination and exceptionally good charge extraction (τ_{rec} >> τ_{ex}) throughout most of the relevant operating conditions of the device. An ability for the blend to retain high *FF* and J_{SC} values despite of a low energetic offset is shown to be due to a beneficial morphology as suggested by pc-AFM, GIWAXS, as well as solid-state ^{19}F MAS NMR and 2D ^{19}F{^{19}F} correlation NMR analyses. The moderate recombination rates in this blend can be explained by the beneficial phase separation between the polymer and NFA, as visualized on a micron-scale by pc-AFM and confirmed on a nm to sub-nm scale by ssNMR. The exceptional extraction in the blend can be attributed to the unencumbered pathways for sweeping out charge carriers via organized PM6 and Y6 domains in the blend. These insights from atomically resolved measurements provide explanations for the moderate recombination and exceptional extraction in the studied devices with *PCE*s of over 15%.

Acknowledgements

A.K. and J.V. contributed equally to this work. This work was supported by the Department of the Navy, Office of Naval Research Award No. N00014-14-1-0580. A.K. acknowledges funding by the Schlumberger foundation. J.V. acknowledges funding by the Alexander-von-Humboldt Stiftung. G. N. M. R. gratefully acknowledges the European Union's Horizon 2020 research and innovation programme under the Marie Skłodowska-Curie grant agreement No. 795091. Financial support from the IR-RMN-THC FR-3050 CNRS France for conducting solid-state NMR measurements is acknowledged. The authors would like to thank Liuyang Zhou and Professor Yingping Zou for advice

with device optimization and Dr. Viktor Brus and Dr. Martin Seifrid for helpful discussions. This research used resources of the Advanced Light Source, which is a DOE Office of Science User Facility under contract no. DE-AC02-05CH11231.

References

[1] Y. Cui, H. Yao, J. Zhang, T. Zhang, Y. Wang, L. Hong, K. Xian, B. Xu, S. Zhang, J. Peng, Z. Wei, F. Gao, J. Hou, *Nature Communications* **2019**, *10*, 2515.

[2] D. Baran, T. Kirchartz, S. Wheeler, S. Dimitrov, M. Abdelsamie, J. Gorman, R. S. Ashraf, S. Holliday, A. Wadsworth, N. Gasparini, P. Kaienburg, H. Yan, A. Amassian, C. J. Brabec, J. R. Durrant, I. McCulloch, *Energy Environ. Sci.* **2016**, *9*, 3783.

[3] J. Liu, S. Chen, D. Qian, B. Gautam, G. Yang, J. Zhao, J. Bergqvist, F. Zhang, W. Ma, H. Ade, O. Inganäs, K. Gundogdu, F. Gao, H. Yan, *Nature Energy* **2016**, *1*, 16089.

[4] C. Sun, F. Pan, H. Bin, J. Zhang, L. Xue, B. Qiu, Z. Wei, Z.-G. Zhang, Y. Li, *Nat Commun* **2018**, *9*, 743.

[5] D. Qian, Z. Zheng, H. Yao, W. Tress, T. R. Hopper, S. Chen, S. Li, J. Liu, S. Chen, J. Zhang, X.-K. Liu, B. Gao, L. Ouyang, Y. Jin, G. Pozina, I. A. Buyanova, W. M. Chen, O. Inganäs, V. Coropceanu, J.-L. Bredas, H. Yan, J. Hou, F. Zhang, A. A. Bakulin, F. Gao, *Nature Materials* **2018**, *17*, 703.

[6] N. A. Ran, J. A. Love, M. C. Heiber, X. Jiao, M. P. Hughes, A. Karki, M. Wang, V. V. Brus, H. Wang, D. Neher, H. Ade, G. C. Bazan, T.-Q. Nguyen, *Advanced Energy Materials* **2018**, *8*, 1701073.

[7] N. A. Ran, J. A. Love, C. J. Takacs, A. Sadhanala, J. K. Beavers, S. D. Collins, Y. Huang, M. Wang, R. H. Friend, G. C. Bazan, T.-Q. Nguyen, *Advanced Materials* **2016**, *28*, 1482.

[8] K. Kawashima, Y. Tamai, H. Ohkita, I. Osaka, K. Takimiya, *Nature Communications* **2015**, *6*, DOI 10.1038/ncomms10085.

[9] F. D. Eisner, M. Azzouzi, Z. Fei, X. Hou, T. D. Anthopoulos, T. J. S. Dennis, M. Heeney, J. Nelson, *J. Am. Chem. Soc.* **2019**, *141*, 6362.

[10] G. Han, Y. Yi, *J. Phys. Chem. Lett.* **2019**, 2911.

[11] J. Yuan, Y. Zhang, L. Zhou, G. Zhang, H.-L. Yip, T.-K. Lau, X. Lu, C. Zhu, H. Peng, P. A. Johnson, M. Leclerc, Y. Cao, J. Ulanski, Y. Li, Y. Zou, *Joule* **2019**, *3*, 1140.

[12] G. F. Burkhard, E. T. Hoke, M. D. McGehee, *Advanced Materials* **2010**, *22*, 3293.

[13] L. Perdigón Toro, H. Zhang, F. Gao, D. Neher, *Unpublished* **2019**.

[14] K. Vandewal, J. Benduhn, V. C. Nikolis, *Sustainable Energy & Fuels* **2018**, *2*, 538.

[15] K. Vandewal, K. Tvingstedt, A. Gadisa, O. Inganäs, J. V. Manca, *Phys. Rev. B* **2010**, *81*, 125204.

[16] S. M. Menke, A. Sadhanala, M. Nikolka, N. A. Ran, M. K. Ravva, S. Abdel-Azeim, H. L. Stern, M. Wang, H. Sirringhaus, T.-Q. Nguyen, J.-L. Brédas, G. C. Bazan, R. H. Friend, *ACS Nano* **2016**, *10*, 10736.

[17] S. M. Tuladhar, M. Azzouzi, F. Delval, J. Yao, A. A. Y. Guilbert, T. Kirchartz, N. F. Montcada, R. Dominguez, F. Langa, E. Palomares, J. Nelson, *ACS Energy Lett.* **2016**, *1*, 302.

[18] N. A. Ran, S. Roland, J. A. Love, V. Savikhin, C. J. Takacs, Y.-T. Fu, H. Li, V. Coropceanu, X. Liu, J.-L. Brédas, G. C. Bazan, M. F. Toney, D. Neher, T.-Q. Nguyen, *Nature Communications* **2017**, *8*, 79.

[19] K. D. Rosenthal, M. P. Hughes, B. R. Luginbuhl, N. A. Ran, A. Karki, S.-J. Ko, H. Hu, M. Wang, H. Ade, T.-Q. Nguyen, *Advanced Energy Materials* **2019**, *9*, 1901077.

[20] U. Rau, *Phys. Rev. B* **2007**, *76*, 085303.

[21] K. Vandewal, K. Tvingstedt, A. Gadisa, O. Inganäs, J. V. Manca, *Nat Mater* **2009**, *8*, 904.

[22] U. Rau, U. W. Paetzold, T. Kirchartz, *Phys. Rev. B* **2014**, *90*, 035211.

[23] J. Benduhn, K. Tvingstedt, F. Piersimoni, S. Ullbrich, Y. Fan, M. Tropiano, K. A. McGarry, O. Zeika, M. K. Riede, C. J. Douglas, S. Barlow, S. R. Marder, D. Neher, D. Spoltore, K. Vandewal, *Nature Energy* **2017**, *2*, 17053.

[24] X.-K. Chen, M. K. Ravva, H. Li, S. M. Ryno, J.-L. Brédas, *Advanced Energy Materials* **2016**, *6*, 1601325.

[25] J. Benduhn, F. Piersimoni, G. Londi, A. Kirch, J. Widmer, C. Koerner, D. Beljonne, D. Neher, D. Spoltore, K. Vandewal, *Advanced Energy Materials* **2018**, *8*, 1800451.

[26] S. D. Collins, C. M. Proctor, N. A. Ran, T.-Q. Nguyen, *Advanced Energy Materials* **2016**, *6*, 1501721.

[27] D. Venkateshvaran, M. Nikolka, A. Sadhanala, V. Lemaur, M. Zelazny, M. Kepa, M. Hurhangee, A. J. Kronemeijer, V. Pecunia, I. Nasrallah, I. Romanov, K. Broch, I. McCulloch, D. Emin, Y. Olivier, J. Cornil, D. Beljonne, H. Sirringhaus, *Nature* **2014**, *515*, 384.

[28] A. Karki, G.-J. A. H. Wetzelaer, G. N. M. Reddy, V. Nádaždy, M. Seifrid, F. Schauer, G. C. Bazan, B. F. Chmelka, P. W. M. Blom, T.-Q. Nguyen, *Advanced Functional Materials* **2019**, *29*, 1901109.

[29] V. C. Nikolis, A. Mischok, B. Siegmund, J. Kublitski, X. Jia, J. Benduhn, U. Hörmann, D. Neher, M. C. Gather, D. Spoltore, K. Vandewal, *Nat Commun* **2019**, *10*, 1.

[30] M. Bixon, J. Jortner, J. W. Verhoeven, *J. Am. Chem. Soc.* **1994**, *116*, 7349.

[31] K. Vandewal, K. Tvingstedt, O. Inganäs, *Phys. Rev. B* **2012**, *86*, 035212.

[32] D. Bartesaghi, I. del C. Pérez, J. Kniepert, S. Roland, M. Turbiez, D. Neher, L. J. A. Koster, *Nature Communications* **2015**, *6*, 7083.

[33] M. C. Heiber, T. Okubo, S.-J. Ko, B. R. Luginbuhl, N. A. Ran, M. Wang, H. Wang, M. A. Uddin, H. Y. Woo, G. C. Bazan, T.-Q. Nguyen, *Energy Environ. Sci.* **2018**, *11*, 3019.

[34] J. Vollbrecht, C. Wiebeler, H. Bock, S. Schumacher, H.-S. Kitzerow, *J. Phys. Chem. C* **2019**, *123*, 4483.

[35] V. V. Brus, C. M. Proctor, N. A. Ran, T.-Q. Nguyen, *Advanced Energy Materials* **2016**, *6*, 1502250.

[36] A. K. K. Kyaw, D. H. Wang, D. Wynands, J. Zhang, T.-Q. Nguyen, G. C. Bazan, A. J. Heeger, *Nano Lett.* **2013**, *13*, 3796.

[37] L. J. A. Koster, V. D. Mihailetchi, H. Xie, P. W. M. Blom, *Appl. Phys. Lett.* **2005**, *87*, 203502.

[38] S. R. Cowan, N. Banerji, W. L. Leong, A. J. Heeger, *Advanced Functional Materials* **2012**, *22*, 1116.

[39] C. M. Proctor, M. Kuik, T.-Q. Nguyen, *Progress in Polymer Science* **2013**, *38*, 1941.

[40] V. V. Brus, *Organic Electronics* **2016**, *29*, 1.

[41] C. M. Proctor, C. Kim, D. Neher, T.-Q. Nguyen, *Advanced Functional Materials* **2013**, *23*, 3584.

[42] J. Vollbrecht, V. V. Brus, S.-J. Ko, J. Lee, A. Karki, D. X. Cao, K. Cho, G. C. Bazan, T.-Q. Nguyen, *Advanced Energy Materials* **n.d.**, *0*, 1901438.

[43] S. Albrecht, J. R. Tumbleston, S. Janietz, I. Dumsch, S. Allard, U. Scherf, H. Ade, D. Neher, *J. Phys. Chem. Lett.* **2014**, *5*, 1131.

[44] V. V. Brus, J. Lee, B. R. Luginbuhl, S.-J. Ko, G. C. Bazan, T.-Q. Nguyen, *Advanced Materials* **2019**, *31*, 1900904.

[45] E. H. Poindexter, P. J. Caplan, B. E. Deal, R. R. Razouk, *Journal of Applied Physics* **1981**, *52*, 879.

[46] R.-Z. Liang, Y. Zhang, V. Savikhin, M. Babics, Z. Kan, M. Wohlfahrt, N. Wehbe, S. Liu, T. Duan, M. F. Toney, F. Laquai, P. M. Beaujuge, *Advanced Energy Materials* **2019**, *9*, 1802836.

[47] A. Armin, J. Subbiah, M. Stolterfoht, S. Shoaee, Z. Xiao, S. Lu, D. J. Jones, P. Meredith, *Advanced Energy Materials* **2016**, *6*, 1600939.

[48] A. Zaban, M. Greenshtein, J. Bisquert, *ChemPhysChem* **2003**, *4*, 859.

[49] J. A. Love, C. M. Proctor, J. Liu, C. J. Takacs, A. Sharenko, T. S. van der Poll, A. J. Heeger, G. C. Bazan, T.-Q. Nguyen, *Advanced Functional Materials* **2013**, *23*, 5019.

[50] J. A. Love, I. Nagao, Y. Huang, M. Kuik, V. Gupta, C. J. Takacs, J. E. Coughlin, L. Qi, T. S. van der Poll, E. J. Kramer, A. J. Heeger, T.-Q. Nguyen, G. C. Bazan, *J. Am. Chem. Soc.* **2014**, *136*, 3597.

[51] X.-D. Dang, A. B. Tamayo, J. Seo, C. V. Hoven, B. Walker, T.-Q. Nguyen, *Advanced Functional Materials* **2010**, *20*, 3314.

[52] M. Guide, X.-D. Dang, T.-Q. Nguyen, *Adv. Mater. Weinheim* **2011**, *23*, 2313.

[53] X. Xu, K. Fukuda, A. Karki, S. Park, H. Kimura, H. Jinno, N. Watanabe, S. Yamamoto, S. Shimomura, D. Kitazawa, T. Yokota, S. Umezu, T.-Q. Nguyen, T. Someya, *PNAS* **2018**, 201801187.

[54] J. Lee, S.-J. Ko, M. Seifrid, H. Lee, B. R. Luginbuhl, A. Karki, M. Ford, K. Rosenthal, K. Cho, T.-Q. Nguyen, G. C. Bazan, *Advanced Energy Materials* **2018**, *8*, 1801212.

[55] S. Mukherjee, C. M. Proctor, G. C. Bazan, T.-Q. Nguyen, H. Ade, *Advanced Energy Materials* **2015**, *5*, 1500877.

[56] C. M. Proctor, S. Albrecht, M. Kuik, D. Neher, T.-Q. Nguyen, *Advanced Energy Materials* **2014**, *4*, 1400230.

[57] B. Walker, A. B. Tamayo, X.-D. Dang, P. Zalar, J. H. Seo, A. Garcia, M. Tantiwiwat, T.-Q. Nguyen, *Advanced Functional Materials* **2009**, *19*, 3063.

[58] N. C. Miller, E. Cho, M. J. N. Junk, R. Gysel, C. Risko, D. Kim, S. Sweetnam, C. E. Miller, L. J. Richter, R. J. Kline, M. Heeney, I. McCulloch, A. Amassian, D. Acevedo-Feliz, C. Knox, M. R. Hansen, D. Dudenko, B. F. Chmelka, M. F. Toney, J.-L. Brédas, M. D. McGehee, *Advanced Materials* **2012**, *24*, 6071.

[59] V. Vohra, K. Kawashima, T. Kakara, T. Koganezawa, I. Osaka, K. Takimiya, H. Murata, *Nature Photonics* **2015**, *9*, 403.

[60] J. R. Tumbleston, B. A. Collins, L. Yang, A. C. Stuart, E. Gann, W. Ma, W. You, H. Ade, *Nature Photonics* **2014**, *8*, 385.

[61] B. P. Rand, D. Cheyns, K. Vasseur, N. C. Giebink, S. Mothy, Y. Yi, V. Coropceanu, D. Beljonne, J. Cornil, J.-L. Brédas, J. Genoe, *Advanced Functional Materials* **2012**, *22*, 2987.

[62] Y. Yi, V. Coropceanu, J.-L. Brédas, *J. Am. Chem. Soc.* **2009**, *131*, 15777.

[63] B. Yang, Y. Yi, C.-R. Zhang, S. G. Aziz, V. Coropceanu, J.-L. Brédas, *J. Phys. Chem. C* **2014**, *118*, 27648.

[64] R. C. Nieuwendaal, D. M. DeLongchamp, L. J. Richter, C. R. Snyder, R. L. Jones, S. Engmann, A. Herzing, M. Heeney, Z. Fei, A. B. Sieval, J. C. Hummelen, *Phys. Rev. Lett.* **2018**, *121*, 026101.

[65] M. R. Hansen, R. Graf, H. W. Spiess, *Chem. Rev.* **2016**, *116*, 1272.

[66] A. Karki, G.-J. A. H. Wetzelaer, G. N. M. Reddy, V. Nádaždy, M. Seifrid, F. Schauer, G. C. Bazan, B. F. Chmelka, P. W. M. Blom, T.-Q. Nguyen, *Advanced Functional Materials* **n.d.**, *0*, 1901109.

[67] A. Melnyk, M. J. N. Junk, M. D. McGehee, B. F. Chmelka, M. R. Hansen, D. Andrienko, *J. Phys. Chem. Lett.* **2017**, *8*, 4155.

[68] M. T. Seifrid, G. N. M. Reddy, C. Zhou, B. F. Chmelka, G. C. Bazan, *J. Am. Chem. Soc.* **2019**, *141*, 5078.

[69] K. R. Graham, C. Cabanetos, J. P. Jahnke, M. N. Idso, A. El Labban, G. O. Ngongang Ndjawa, T. Heumueller, K. Vandewal, A. Salleo, B. F. Chmelka, A. Amassian, P. M. Beaujuge, M. D. McGehee, *J. Am. Chem. Soc.* **2014**, *136*, 9608.

[70] B. Elena, G. Pintacuda, N. Mifsud, L. Emsley, *J. Am. Chem. Soc.* **2006**, *128*, 9555.

Unraveling the High Performance of over 15 % Efficiency in Single-Junction Bulk Heterojunction Organic Solar Cells

A.K., J. V., A. L. D., N. S., M. S., G. N. M. R.*, T.-Q. N.*

SHORT ABSTRACT:

The high performing single-junction organic solar cell blend, PM6:Y6, was examined to obtain an in-depth understanding of the voltage losses, and charge recombination and extraction dynamics. The devices exhibit remarkable extraction coupled with moderate recombination losses. This behavior can most likely be credited to a beneficial morphology as evidenced by atomically resolved ^{19}F magic-angle spinning solid-state NMR analyses.

ToC figure ((Please choose one size: 55 mm broad × 50 mm high or 110 mm broad × 20 mm high. Please do not use any other dimensions))